

Original article

Spontaneous imbibition behavior in porous media with various hydraulic fracture propagations: A pore-scale perspective

Yan Zhou¹, Wei Guan¹^{*}, Changming Zhao², Xiaojing Zou¹, Zhennan He³, Hongyang Zhao⁴

¹Department of Astronautics and Mechanics, Harbin Institute of Technology, Harbin 150001, P. R. China

²Oil Production Engineering Research Institute of Daqing Oilfield Co. Ltd, Daqing 163000, P. R. China

³School of Energy and Power Engineering, Shandong University, Jinan 250061, P. R. China

⁴Beijing Oil & Gas Transportation Center, PipeChina, Beijing 100013, P. R. China

Keywords:

Pore-scale modeling
porous media
spontaneous imbibition
fracture propagation

Cited as:

Zhou, Y., Guan, W., Zhao, C., Zou, X., He, Z., Zhao, H. Spontaneous imbibition behavior in porous media with various hydraulic fracture propagations: A pore-scale perspective. *Advances in Geo-Energy Research*, 2023, 9(3): 185-197.

<https://doi.org/10.46690/ager.2023.09.06>

Abstract:

Hydraulic fracturing technology can improve the geologic structure of unconventional oil and gas reservoirs, yielding a complex fracture network resulting from the synergistic action of hydraulic and natural fractures. However, the impact of spontaneous imbibition associated with hydraulic fracture propagation on the reservoir matrix remains poorly understood. In this study, combining the Cahn-Hilliard phase field method with the Navier-Stokes equations, pore-scale modeling was employed to capture the evolution of the oil-water interface during dynamic spontaneous imbibition for hydraulic fracture propagation in a two-end open mode. This pore-scale modeling approach can effectively circumvent the challenges of conducting spontaneous imbibition experiments on specimens partitioned by hydraulic fractures. A direct correlation was established between the pressure difference curve and the morphology of discharged oil phase in the primary hydraulic fracture, providing valuable insights into the distribution of oil phase in spontaneous imbibition. Furthermore, it was shown that secondary hydraulic fracture propagation expands the longitudinal swept area and enhances the utilization of natural fractures in the transverse swept area during spontaneous imbibition. When secondary hydraulic fracture propagation results in the interconnection of upper and lower primary hydraulic fractures, competitive imbibition occurs in the matrix, leading to reduced oil recovery compared to the unconnected models. Our results shed light upon the spontaneous imbibition mechanism in porous media with hydraulic fracture propagation, contributing to the refinement and application of hydraulic fracturing techniques.

1. Introduction

With the development of unconventional oil reservoirs, hydraulic fracturing has emerged as the primary technique for reservoir exploitation (Li et al., 2019b; Yang and Liu, 2021). This strategy effectively reforms the reservoir structure. Compared to conventional fractured reservoirs, reformed reservoirs have more complex fracture structures due to the influence of hydraulic fracture propagations (Fig. 1) (Gruener et al., 2012; Zhang et al., 2021). Spontaneous imbibition, as a critical mechanism for enhancing oil recovery in fractured reservoirs, is strongly influenced by the fracture structure (Cai and

Yu, 2012; Cai et al., 2014; Li et al., 2019a). Understanding the role of various hydraulic fracture propagation phenomena during spontaneous imbibition can provide valuable insights into reservoir development.

In order to investigate the contribution of spontaneous imbibition to enhanced oil recovery, theoretical analyses and laboratory experiments have been conducted since the discovery of this phenomenon by Brownscombe and Dyes (1952). Several factors influencing spontaneous imbibition, such as core geometric properties, core physical properties, fluid properties, and wettability, have been discussed (Hatiboglu et al., 2007; Yang et al., 2019; Cai et al., 2020; Guo et al., 2020; He et

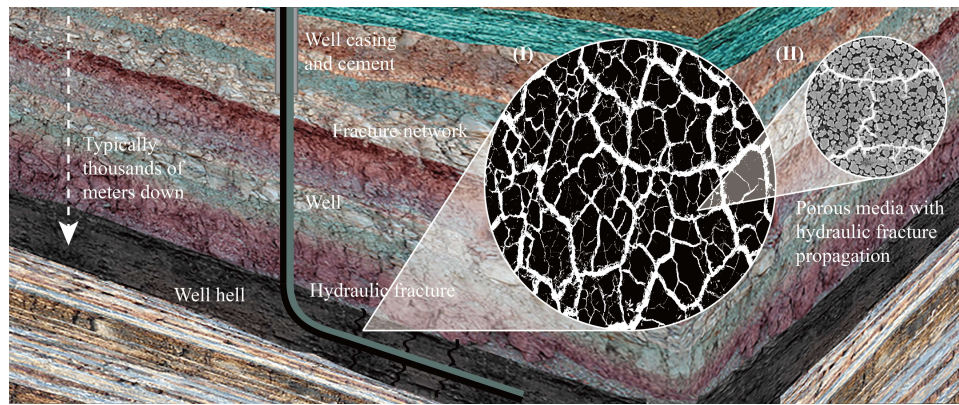


Fig. 1. Schematic illustration of hydraulic fracturing in an oil reservoir. The cross-sections show (I) a complex fracture system resulting from hydraulic fracturing and (II) the propagation of primary and secondary hydraulic fractures within porous media.

al., 2022b). Unfortunately, with the research expanding to the core-scale, these works have faced challenges in considering the microscale pore structure and internal flow details. The reason is that scholars have treated the permeability domain of porous medium as a “black-box” model and described the flow within the porous medium at the macroscopic scale by combining Darcy’s law and measuring parameters such as pressure difference, flow rate, etc.

With recent breakthroughs in imaging technology, microscale experiments regarding the observation and characterization of microstructure and fluid transport in porous media have been facilitated (Cai and Yu, 2012; Lee et al., 2019). These experiments achieved the visualization of flow, which is difficult for theoretical analysis and laboratory experiments (Narsilio et al., 2009; Gao et al., 2018; Liu et al., 2022; Liang et al., 2023). Sinton (2004) indicated that a variety of methods could be established for microscale flow visualization that can link to macroflow visualization methods, and the physical mechanisms underlying these methods were explained. Lei et al. (2022) implemented the microscale flow visualization method to find that suspensions with moderate microgel-in-oil content could achieve the strongest sweeping and carrying abilities that contribute to the highest displacement efficiency. However, some complex boundaries could not be realized because of the experimental conditions (Xiong et al., 2016; Zhou et al., 2022). For example, in hydraulic fracturing experiments at the core scale, only experimental samples that are not penetrated by hydraulic fractures can be obtained because the penetrated samples are split into two separate samples. This makes it more challenging to study the fluid transport of spontaneous imbibition in porous media with hydraulic fracture propagation.

In order to overcome the challenges of sample and imbibition boundary, pore-scale numerical simulations have emerged as a significant tool for investigating the microscale flow mechanisms in reservoirs, in addition to physical laboratory experiments (Cai et al., 2010; Berg et al., 2013; Blunt et al., 2013; Berg and van Wunnik, 2017). Currently, pore-scale models for calculating spontaneous imbibition by solving the Navier-Stokes equations may be divided into two main categories, namely, direct numerical simulations and lattice

Boltzmann methods (Pooladi-Darvish and Firoozabadi, 2000). These can visualize the velocity and pressure fields throughout the pore space, which are difficult to obtain experimentally (Liu et al., 2021; He et al., 2023; Wang et al., 2023). For example, Jafari et al. (2017) investigated the effects of water injection rate, fracture aperture and grain geometry on spontaneous percolation in a porous medium without fracture. Subsequently, several scholars conducted related studies considering porous media with fracture. Liu et al. (2020) and He et al. (2022a) employed spontaneous imbibition in a spherical stacking model and a real core pore using the color-fluid lattice Boltzmann and the phase-field method, respectively. Zhu et al. (2021) investigated the effects of fracture width, bifurcation angle, tortuosity, and water flow rate on spontaneous imbibition. Previous spontaneous imbibition studies typically rely on a single imbibition boundary, while actual hydraulic fracturing results in a complex fracture boundary. Therefore, due to the inapplicability of a single seepage boundary and the complex mechanism of hydraulic fracture propagation, it is imperative to conduct further studies on the effect of fracture propagation on spontaneous imbibition.

This study investigated the effects of various the hydraulic fracture propagations on spontaneous imbibition in porous media from a pore-scale perspective. In contrast to previous research, our focus was on considering two cases of hydraulic fracture extension in porous media in the two-end open mode: (1) without natural fractures and (2) with natural fractures. The remaining sections of this study were organized as follows. First, the governing equations, model generation by thresholding Gaussian random fields, and validation of pore-scale numerical simulation were briefly described. Then, using systematic comparison, the effects of hydraulic fracture propagation on interfacial evolution in the primary hydraulic fractures and matrix and oil recovery were analyzed. Finally, the main conclusions were summarized.

2. Numerical model

2.1 Porous model reconstruction

This study used the threshold Gaussian random field method to obtain realistic features of the pore space used for

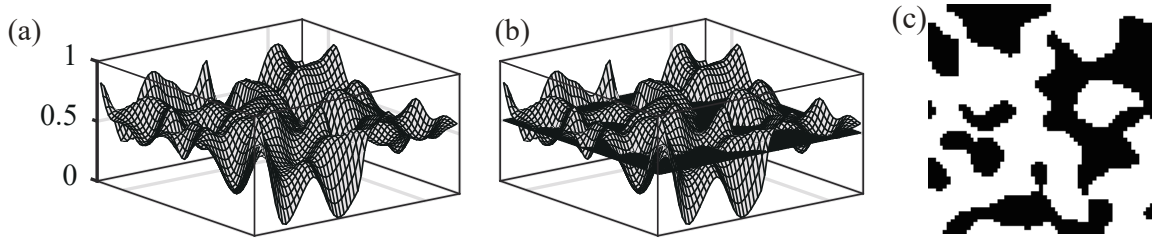


Fig. 2. An example of porous media using the threshold Gaussian random field method. (a) Related Gaussian field; (b) segmentation using thresholds and (c) two-dimensional pore structure generated after threshold segmentation.

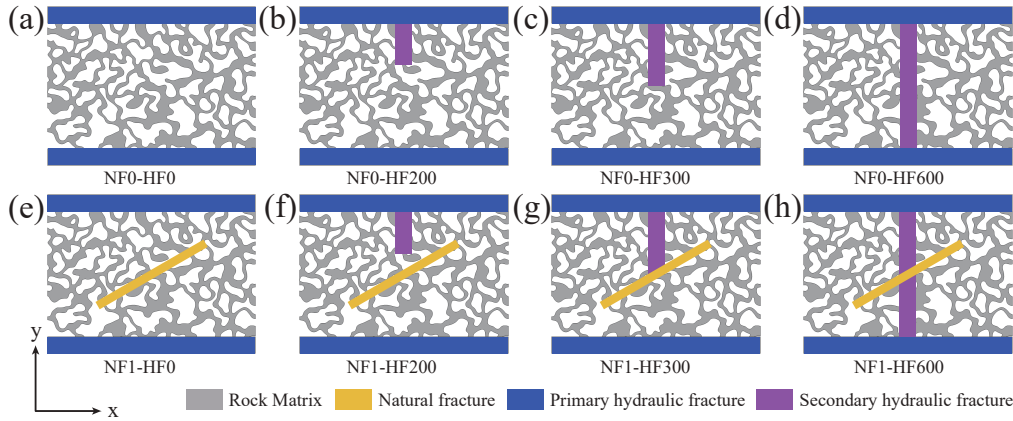


Fig. 3. Schematic diagram of geometric structure. The rock matrix of all models was generated in a $1000 \times 600 \mu\text{m}^2$ two-dimensional domain. The size of the upper and lower primary hydraulic fractures in all models was $1000 \times 80 \mu\text{m}^2$. The length of secondary hydraulic fractures in the (a) NF0-HF0, (b) NF0-HF200, (c) NF0-HF300 and (d) NF0-HF600 models were $0 \mu\text{m}$, $200 \mu\text{m}$, $300 \mu\text{m}$, and $600 \mu\text{m}$, respectively. The (e) NF1-HF0, (f) NF1-HF200, (g) NF1-HF300 and (h) NF1-HF600 models correspond to the above models one by one, except for the natural fracture with a size of $600 \times 30 \mu\text{m}^2$ and an inclination of 30° .

numerical experiments (Hyman and Winter, 2014; Robertson and Kalidindi, 2022). This method, as demonstrated by Hyman and Winter (2014), could generate pore structures with specific correlation characteristics. It consists of three steps that create a random domain $u(\mathbf{x})$ (Fig. 2(a)), a Gaussian random field $T(\mathbf{x})$ (Fig. 2(b)), and a pore space $P(\mathbf{x})$ (Fig. 2(c)). The elements in $u(\mathbf{x})$ were treated as independent, identically distributed random variables sampled from a continuous uniform distribution spanning the interval $[a, b]$. The realization of $T(\mathbf{x})$ was achieved by convolving a deterministic convolution kernel, designated as $k(\mathbf{x})$, with $u(\mathbf{x})$. For the convolution kernel, Hyman and Winter (2014) pointed out the three examples, including uniform weighting over a finite rectilinear domain, symmetric Gaussian kernels that weigh contributions to the topography by distance from the center point, which decays exponentially with distance, and a symmetric kernel produced by iterative sweeps of a low-pass filter, all of which yield topographies that are normally distributed. Therefore, the Gaussian convolution kernel was selected:

$$k(\mathbf{x}) = \frac{1}{2\pi\sigma^2} \exp\left(-\frac{\mathbf{x}^2 + \mathbf{y}^2}{2\sigma^2}\right) \quad (1)$$

$$T(\mathbf{x}) = \int_{R^2} k(\mathbf{x} - \mathbf{y})u(\mathbf{y})d\mathbf{y} \quad (2)$$

For computational convenience, one needs to ensure that $\int_{R^2} k(\mathbf{x})d\mathbf{x} = 1$. Finally, the pore space $P(\mathbf{x})$ is generated by applying a horizontal threshold δ to the Gaussian field $T(\mathbf{x})$:

$$P(\mathbf{x}) = \begin{cases} 0, & \text{if } T(\mathbf{x}) \geq \delta \\ 1, & \text{if } T(\mathbf{x}) < \delta \end{cases} \quad (3)$$

where $P(\mathbf{x}) = 1$ represents the pore space and $P(\mathbf{x}) = 0$ represents the solid matrix. Notably, the topology and geometry of the pore space are dependent on $k(\mathbf{x})$ and δ . Here, $k(\mathbf{x})$ is regulated by the length dimension θ , which determines the correlation structure of the pore space, and the threshold finally determines the pore space. Rigorous theoretical analysis has proved that the specific choices of θ and δ can generate pore spaces that conform to the desired Minkowski generalized values.

Referring to the work of He et al. (2022a), a porous medium was generated with a porosity of 0.45 in a two-dimensional (2D) domain by selecting the parameters $\theta = 110^{-8} \text{ m}^2$ and $\delta = 0.45$, as shown in the gray part of Fig. 3. Considering the two-end open mode in spontaneous imbi-

tion, the two parallel rectangles were added on the top and bottom sides of the model to represent the primary hydraulic fracture. In addition, a rectangle with an inclination angle was prefabricated to represent the natural fracture in the matrix. In the results of previous studies, the intersection of hydraulic and natural fractures shows different fracture propagation patterns according to the intersecting action criterion (Dahi et al., 2016; Kolawole and Ispas, 2020; Li et al., 2023). Therefore, four cases were selected as the research working conditions in this study: (1) no secondary hydraulic fracture extension occurs; (2) the secondary hydraulic fracture extends but does not reach the natural fracture; (3) the secondary hydraulic fracture extends and touches the natural fracture and turns at the end of the natural fracture; and (4) the secondary hydraulic fracture passes through the natural fracture and links the two primary fractures. To investigate the effects of natural fractures in spontaneous percolation, the above models were replicated accurately, except for the deletion of the natural fractures. This operation ensured that the geometric features were identical except for the focus of this study.

Both phase field methods and level sets are commonly used numerical methods to solve the fluid flow behavior in porous media. In contrast to the level-set approach, the phase field method has significant advantages in handling complex geometric shapes and multiphase domains (Prodanović and Bryant, 2006). This advantage comes from implicitly describing the position and evolution of phase interfaces by the phase field function, thus avoiding explicit tracking. The level-set method uses a level-set function governed by the Hamilton-Jacobi equation to represent the positions and shapes of phase interfaces. Consequently, in contrast to the level-set method, the interface evolution described by the phase field method exhibits smoothness. Detailed comparisons between the phase field and level-set methods can be found in the work of Akhlaghi and Hamouda (2013). Therefore, the Cahn–Hilliard phase field method coupled with the Navier–Stokes and continuity equations was used to simulate dynamic spontaneous imbibition. First, the Navier-Stokes equation with surface tension as a volume force and continuity equations were added to describe the fluid flow within a porous medium:

$$\rho \frac{\partial \mathbf{u}}{\partial t} + \rho (\mathbf{u} \cdot \nabla) \mathbf{u} = -\nabla p + \nabla \cdot [\mu (\nabla \mathbf{u} + \nabla \mathbf{u}^T)] + F_{st} \quad (4)$$

$$\nabla \cdot \mathbf{u} = 0 \quad (5)$$

where p represents the pressure, Pa; \mathbf{u} represents the velocity vector, m/s; ρ represents the fluid density, kg/m³; μ represents the fluid dynamic viscosity, Pa·s; t is the time, s; and F_{st} is the surface tension force, N/m³. Next, the interface evolution and the dynamical behavior of the phase interface were described by the phase field equations:

$$\frac{\partial \phi}{\partial t} + \mathbf{u} \cdot \nabla \phi = \nabla \cdot \left(\frac{\gamma \lambda}{\varepsilon^2} \right) \nabla \psi \quad (6)$$

$$\psi = -\nabla \cdot \varepsilon^2 \nabla \phi + (\phi^2 - 1) \phi \quad (7)$$

where $\gamma = \chi \varepsilon^2$ is the mobility, representing the migration speed of the interface in unit driving force; χ denotes the

mobility tuning parameter, m·s/kg; and ε is the variable for controlling the interface thickness, m. Following the sensitivity study by Amiri (2014), χ was set to 1 m·s/kg to obtain a smaller volume shrinkage, while the value of ε was set to the maximum grid cell size at the location of the two-phase interface. The phase field method uses the phase-field function ϕ as a variable that describes the continuous variation of the phase interfaces from -1 to 1, blurring the phase interface into a continuous transition region. For the oil-water two-phase, fluid 1 represents the oil phase, fluid 2 represents the water phase, and the interval between -1 and 1 represents the oil-water interface:

$$\begin{cases} \phi(x, t) = -1 & \text{Fluid 1} \\ \phi(x, t) \in (0, 1) & \text{Phase interface} \\ \phi(x, t) = 1 & \text{Fluid 2} \end{cases} \quad (8)$$

The mixing energy density λ as a parameter in the phase field equation was used to characterize surface tension coefficient σ between the oil and the water combined with the parameter ε :

$$\sigma = \frac{2\sqrt{2}\lambda}{3\varepsilon} \quad (9)$$

2.2 Pore-scale modeling

The surface tension was obtained by combining the chemical potentials ψ and phase field function ϕ in the system, thereby realizing the coupling of phase field equations and the Navier-Stokes equations:

$$F_{st} = \frac{\lambda}{\varepsilon^2} \psi \nabla \phi \quad (10)$$

Meanwhile, the wetted wall boundary acts as a key component of the two-phase flow in the porous media. The detailed description is as follows:

$$\mathbf{n} \cdot \varepsilon^2 \nabla \phi = \varepsilon^2 \cos(\theta) |\nabla \phi| \quad (11)$$

$$\mathbf{n} \cdot \frac{\gamma \lambda}{\varepsilon^2} \nabla \psi = 0 \quad (12)$$

where \mathbf{n} represents the unit normal to the wall; and θ is the contact angle, °.

The finite element method was used to solve the established mathematical model. The left and right edges of the primary fractures located at the upper and lower of the model were set as velocity inlet and pressure outlet boundaries, respectively. The interior of the model was set as a wetted wall boundary. The determination of fluid parameters draws on previous relevant studies by He et al. (2022a), and the specific setup parameters were shown in Table 1. Meanwhile, the porosity and permeability of all models were listed in Table 2. In the initial state, the primary fracture is filled with the water phase, while the pore space is saturated with the oil phase. Notably, in addition to the boundary conditions and fluid parameters, the settings for the interface thickness ε and the mobility tuning parameter χ referred to the sensitivity studies performed by Rokhforouz and Akhlaghi Amiri (2019) to ensure the convergence of the model and the accuracy of

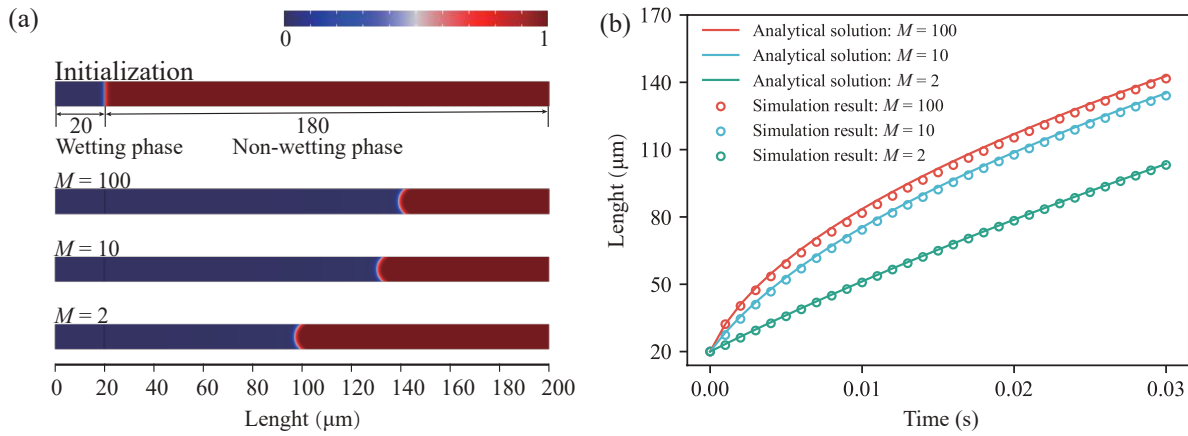


Fig. 4. Verification of phase field method predictions for the dynamic capillary imbibition test: (a) schematic representation of the simulation geometry and the interfacial evolution of capillary imbibition at $M = 2, 10, 100$ and (b) length of the wetting-phase as a function of time for three viscosity ratios M .

Table 1. Fluid Properties.

Fluid	Density (kg/m^3)	Viscosity (mPa·s)	Interfacial tension (N/m)	Contact angle ($^\circ$)
Water	1000	1	0.025	30
Oil	800	6.7		

Table 2. Porosity and permeability of all models.

Number	Porosity	Permeability ($\times 10^{-12} \text{ m}^2$)
NF0-HF0	0.447	3.98
NF0-HF200	0.462	4.16
NF0-HF300	0.470	4.32
NF0-HF600	0.491	4.50
NF1-HF0	0.473	6.38
NF1-HF200	0.489	6.46
NF1-HF300	0.495	6.58
NF1-HF600	0.514	6.94

the phase interface. The geometric model was discretized with a free triangular mesh, and local mesh refinement was performed in the primary and secondary fractures to ensure the accuracy, stability and interface clarity of the calculations. The mesh quality test showed that the number of meshes in the NF0-HF0 model was 257,854, with an average quality of 0.8536. All the calculation cases were computed on a mobile Workstation (Intel Xeon w72495X, Processor 45M Cache, 2.50 GHz), totaling 356.8 h.

2.3 Phase-field method verification

In order to verify the correctness of the phase-field method in spontaneous imbibition, capillary imbibition experiments were performed on a two-dimensional geometry. These experiments are widely used as a typical case of spontaneous imbibition to assess the ability of a multiphase flow model to

describe moving interface problems. The relationship between length L and time t during the dynamic process of spontaneous imbibition for a capillary by a wetting fluid, while neglecting gravitational and inertial forces, was first proposed by Lucas and Washburn (Lucas, 1918; Washburn, 1921):

$$\frac{\mu_w - \mu_{nw}}{2} (l^2 - l_0^2) + \mu_{nw} L(l - l_0) = \frac{R\sigma \cos \theta}{6} t \quad (13)$$

where μ_w and μ_{nw} represent the dynamic viscosities of the wetting and non-wetting phases, respectively; l and R denote the length and radius of the capillary, respectively. In the validation cases, the computational domain contains the $20 \times 10 \mu\text{m}^2$ wetted phase domain and the $180 \times 10 \mu\text{m}^2$ non-wetted phase domain. The left and right boundaries were set as velocity inlet and pressure outlet to maintain the supply of the wetting phase and the timely discharge of the nonwetting phase, respectively. Notably, the velocity of the inlet was 0 m/s. By varying the fluid viscosity of the non-wetting phase, the capillary imbibition process was simulated for three cases with viscosity ratios M of 2, 10 and 100, respectively. Other fluid parameters were fixed: an interfacial tension of 0.025 N/m and a contact angle of 36° . By decreasing the viscosity ratio-while keeping in mind that the viscosity of the wetting fluid remains unchanged-more non-wetting fluid ahead of the interface contributes to viscous dissipation, which slows down the intruding fluid column. The simulation and analytical solution results showed good agreement at all three viscosity ratios, as illustrated in Fig. 4, verifying that the phase-field method is effective in dealing with such problems. Meanwhile, a similar validation using the Hartmann-Poiseuille flow has been performed in our previous study (Zhou et al., 2023).

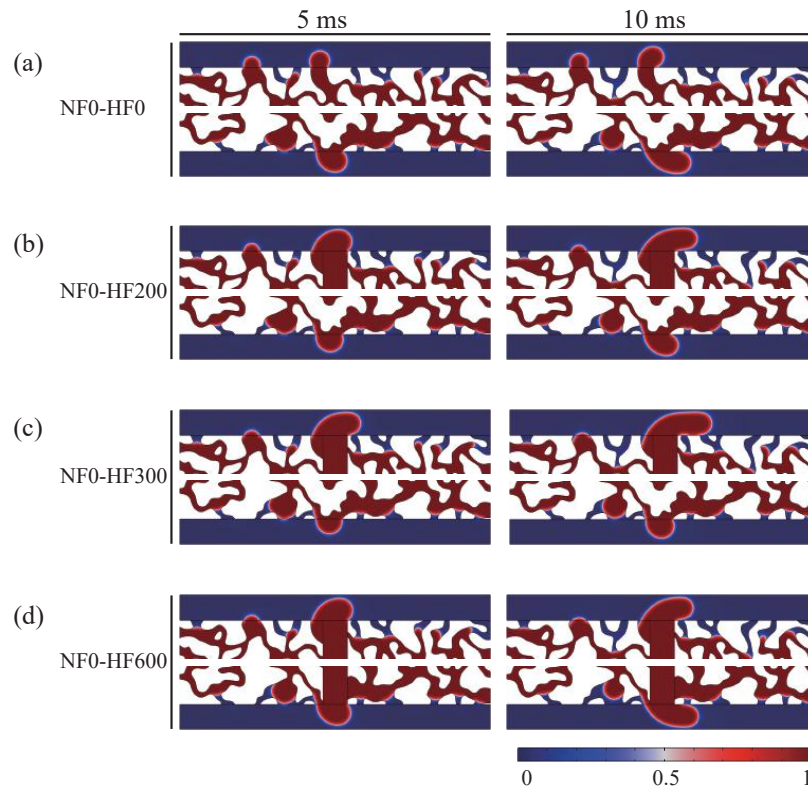


Fig. 5. Interfacial evolution of two-phase fluid in the primary hydraulic fractures in the (a) NF0-HF0, (b) NF0-HF200, (c) NF0-HF300 and (d) NF0-HF600 models at the time points of 5 ms and 10 ms.

3. Simulation and analysis

3.1 Interfacial evolution in primary hydraulic fractures

Primary hydraulic fractures serve as the main transport channels for the discharged oil phase, in which the interfacial evolution and differential pressure curves comprise the key information to reflect the spontaneous imbibition process. Therefore, in this work, the effects of secondary hydraulic fractures on spontaneous imbibition were described by the interfacial evolution of the primary hydraulic fracture in the initial stage, and the relationships between differential pressure and interfacial evolution were elucidated through comparative analyses.

According to the calculation results, in the initial stage of spontaneous imbibition, the swept area of the oil-water interface does not involve the area where the natural fractures are located because the seepage only occurs in the surface area at the interface between the matrix and the primary hydraulic fracture. The presence or absence of natural fractures does not affect the interfacial evolution in the primary hydraulic fracture during the initial stage. Therefore, only the phase interface distribution for models without natural fracture but with different secondary fracture propagations were presented in Fig. 5. As can be seen in the figure, the imbibition meniscus was formed in the small pore space, in contrast to the drainage meniscus formed in the large pore space. According to the Young-Laplace equation, capillary force as a driving force promotes

the preferential drainage of oil phase through large pores since the interfacial properties of the inner surface of the matrix are water-wet. This phenomenon was also observed in the study by Liu et al. (2020) and He et al. (2022a). We compared the development of drainage meniscus of different models and found that the propagations of secondary hydraulic fractures played a positive role. By comparing Figs. 5(a), 5(b) and 5(c), the propagation distances of secondary hydraulic fracture influenced the development rate of the drainage meniscus with a positive correlation. Interestingly, in the NF0-HF600 model, the drainage meniscus contracted in the upper primary hydraulic fracture compared to the NF0-HF200 and NF0-HF300 models, but the drainage meniscus in the lower primary fracture was better developed. The reason for this is that, if gravity is neglected, the capillary force works on the two ends of the secondary fracture simultaneously but in opposite directions. To summarize, the secondary hydraulic fracture propagations indirectly widened the contact area between the flow channel and the matrix, greatly contributing to the imbibition capacity. The oil phase can flow not only through the large pore spaces in direct contact with the primary hydraulic fracture but also into the secondary hydraulic fracture and then through the secondary hydraulic fracture into the primary hydraulic fracture for discharge.

Fig. 6 shows the pressure differences between the two ends of the upper and lower primary hydraulic fractures in each model during the dynamic spontaneous imbibition. To analyze the effect of natural fractures on spontaneous imbibition, the

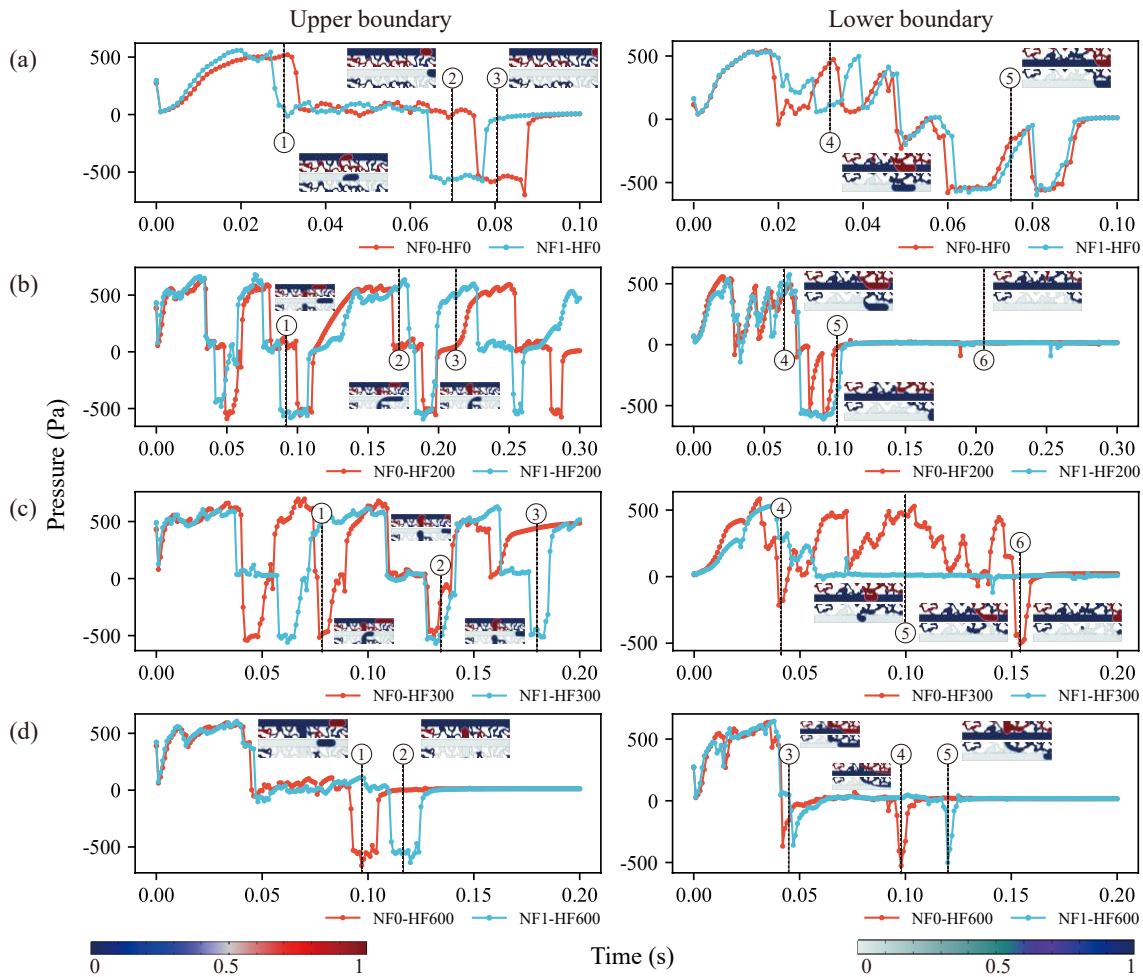


Fig. 6. The pressure difference in the upper and lower primary hydraulic fractures as a function of imbibition time for the all models and the corresponding interface evolution.

pressure difference curves of the presence or absence of natural fractures were plotted in the same figure. To determine the interfacial evolution of the primary hydraulic fracture, the locations of typical differences were labeled. From the pressure difference curve results, three main cases of pressure difference fluctuations could be observed, namely, positive values, 0, and negative values. First, the interfacial evolution of the primary hydraulic fracture shows that the differential pressure curve rises and has positive values when the link between the discharged oil phase and the oil phase in the matrix. The reason is the rise in differential pressure due to the surface tension of the fluid that behaves as a blocking force for the discharged oil phase to satisfy the constant flow rate in the primary hydraulic fracture. This phenomenon is indicated in Fig. 6(a) by markers 1 and 5, Fig. 6(b) by markers 2 and 4, and Fig. 6(c) by markers 1, 3, 4, and 5. As the discharged oil phase enters the primary hydraulic fracture as a whole, it is split and disconnected from the oil phase in the matrix. This phenomenon is manifested as the pressure difference curve value being higher than baseline 0

and fluctuating nearby. This is because the capillary force on the discharged oil phase is the driving force within the primary hydraulic fracture, accelerating the flow speed and advancing the non-wetting water phase, resulting in an overall force balance. This phenomenon is indicated in Fig. 6(b) by markers 1 and 2, and Fig. 6(d) by markers 1. In addition, the pressure difference curves also fluctuated around the baseline 0 when there is no discharged oil phase in the primary hydraulic fracture. This phenomenon is indicated in Fig. 6(a) by markers 3, Fig. 6(b) by markers 1, 3 and 6, and Fig. 6(d) by markers 2, 4 and 5. The pressure difference curves decreased sharply and became negative values when the discharged oil phase moved near the outlet. The reason is that the discharged oil phase does not need to overcome the capillary forces caused by the non-wetting water phase. This phenomenon is indicated in Fig. 6(a) by markers 2, 3, 5, Fig. 6(b) by markers 1 and 5, Fig. 6(c) by markers 1, 2, 3 and 6, and Fig. 6(d) by markers 1, 3 and 4. Therefore, the dynamic spontaneous imbibition can be judged by the fluctuation of the pressure difference curve.

Based on the characteristics of the pressure difference

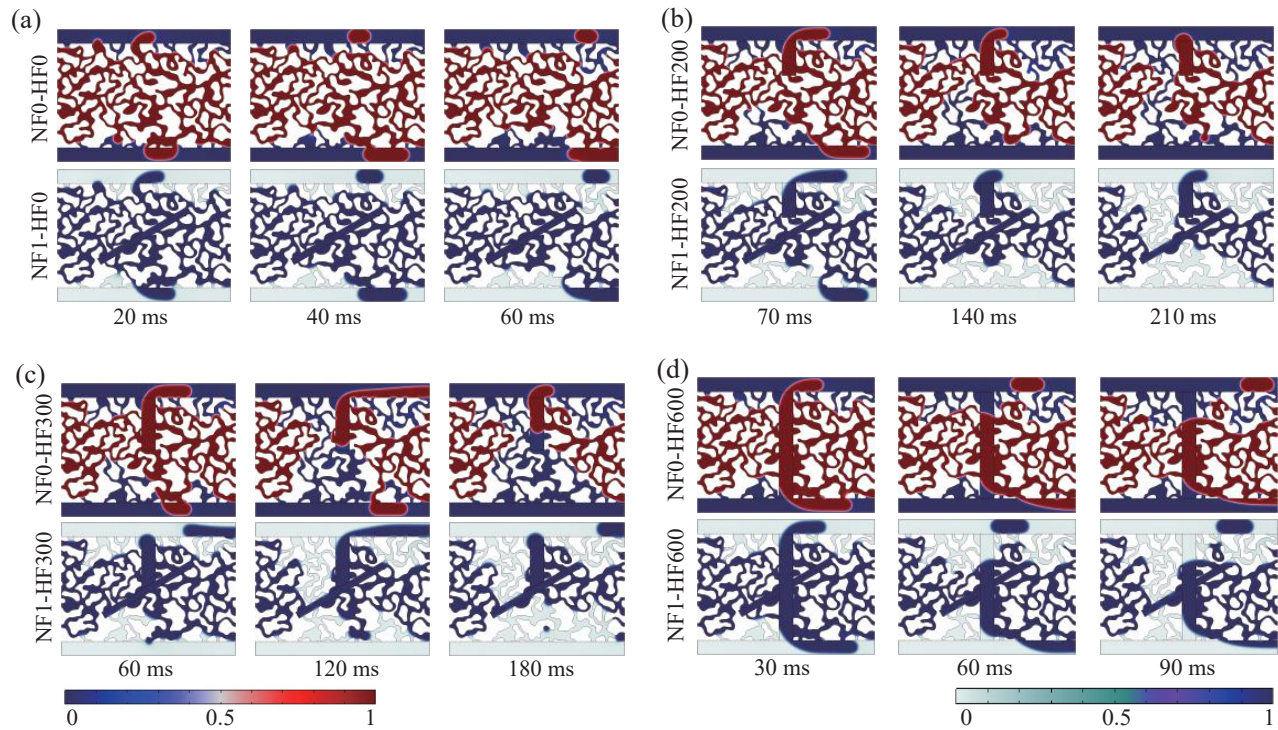


Fig. 7. Interface evolution differences between the same secondary hydraulic fracture propagation fractures and the same time, using the natural fracture as a differentiation criterion.

curve fluctuations, the effects of natural fractures on spontaneous imbibition were analyzed. The part of the pressure difference curve greater than 0 for the NF1-NF0 model with natural fracture appears to decrease at 20-40 ms compared to the NF0-NF0 model without natural fracture, as shown in the upper primary hydraulic fracture in Fig. 6(a). This indicates that the natural fracture impedes spontaneous imbibition. Nevertheless, natural fractures accelerated the migration of the oil phase in the primary hydraulic fracture. The pressure difference curve in the upper primary hydraulic fracture, as shown in Fig. 6(a), shows only frequency changes and no significant changes for the pressure difference curve greater than 0. As the secondary hydraulic fracture propagated, the duration of greater than 0 in the pressure difference curves increased, as shown in Figs. 6(b) and 6(c). This phenomenon illustrates that the secondary hydraulic fractures communicate the hydraulic conductivity of the natural fracture, allowing better drainage of the oil phase. Simultaneously, the secondary hydraulic fractures and natural fractures facilitated the drainage of the oil phase from the upper primary hydraulic fracture. When the propagation of hydraulic fracture resulted in the linking of upper and lower primary hydraulic fractures, the drainage time of oil phase was prolonged, and the drainage volume was increased compared with the NF0-NF0 and NF1-NF0 models, as shown in Fig. 6(d). However, competitive imbibition and discharge retardation occurred during oil phase suction due to the primary hydraulic fracture being communicated. Durations of greater than 0 in the pressure difference curves were reduced compared to NF0-NF200, NF1-NF200, NF0-NF300, and NF1-

NF300. In summary, spontaneous imbibition from a reservoir can be greatly enhanced when hydraulic fracture propagations occur near natural fractures.

3.2 Interfacial evolution in matrixes

The interface evolution of the two-phase fluid within the matrixes significantly differed because of the variability in natural fractures and the propagation of secondary hydraulic fractures. The interfacial evolution of the two-phase fluids in the NF0-HF0 and NF1-HF0 models showed that spontaneous imbibition was weak, as shown in Fig. 7(a). The intrusion interface of the water phase in the matrixes existed at the surface, contacting the primary fracture and the matrix, where the imbibition depth is limited. When analyzing the pressure difference curves, the natural fractures could be seen to accelerate the migration of the discharged oil phase, which was observed in the interfacial evolution of these two models. With the propagation of secondary hydraulic fractures, the capacity of spontaneous imbibition for the matrixes was greatly enhanced, as shown in Fig. 7(b). The propagation of secondary hydraulic fracture allowed the deeper oil phase in the matrix to enter along the secondary hydraulic fracture and was discharged into the primary hydraulic fracture. Moreover, as the oil phase was discharged from the matrix, the water phase from the lower primary hydraulic fracture was more readily accessed inside the matrix, driving the lower oil phase into the secondary hydraulic fracture and increasing the oil recovery. Comparing NF0-HF200 and NF1-HF200 models, natural fractures extended the imbibition of the oil phase in

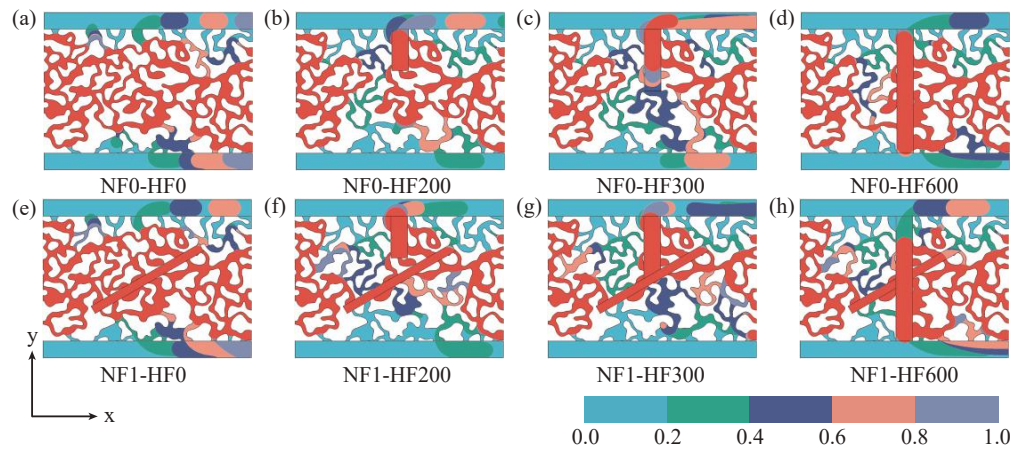


Fig. 8. Interface evolutions with a normalized time interval of 0.2 s. The termination time of the simulation for the spontaneous imbibition for the (a) NF0-HF0, (b) NF0-HF200, (c) NF0-HF300, (d) NF0-HF600, (e) NF1-HF0, (f) NF1-HF200, (g) NF1-HF300 and (h) NF1-HF600 models are 100, 300, 200, 200, 200, 100, 350, 320, 300 and 160 ms, respectively.

the transverse direction.

As the hydraulic fracture propagated further, the water phase interface within the matrix developed further and more oil phase was discharged, as shown in Fig. 7(c). Compared to the NF0-HF200 model, the swept depth became deeper. Meanwhile, comparing the NF1-HF200 model, the transverse swept area of the NF1-HF300 model was expanded further. Most of the oil phase in the area near secondary hydraulic fractures and natural fractures was discharged. However, in the NF0-HF600 and NF1-HF600 models, the oil phase retained a dynamic equilibrium in the secondary hydraulic fractures due to the competitive imbibition mentioned in subsection 3.1. An interesting phenomenon is that most residual oil phases are mostly distributed on the right of the matrix, according to Fig. 7(d). The reason is that the pressure gradient on the left side is greater than on the right side, and the oil phase on the left side is more easily discharged.

The variability of the interface evolution of each model in normalized time could be observed, as shown in Fig. 8. The overall interfacial evolution shows that hydraulic fracture propagations effectively promote the drainage of the oil phase in the matrixes. The imbibition interfaces were predominantly located in the matrix, and the drainage interfaces were mainly located in secondary hydraulic and natural fractures. Differences in the matrix structure did not affect interfacial evolution in the initial stage with normalization times of 0-0.2 s. At normalization times between 0.2 and 0.4 s, the variability of the interfacial evolution brought about by the matrix structure began to emerge. Comparing the differences in interfacial evolution between each model, certain phenomena could be observed, such as the previously described hydraulic fracture propagations increasing the swept area and depth and the natural fractures effectively extending the transverse swept area. The main discharge of oil phases was concentrated in the first four normalized time intervals. At the last normalization time interval, the oil recovery efficiency decreased and gradually stabilized. In particular, in the NF0-HF600 and NF1-HF600

models, the interface did not evolve and the overall models were in dynamic equilibrium. This phenomenon demonstrates that reducing the trans-layer in hydraulic fracturing can effectively improve the oil recovery of the reservoir through the reasonable selection of perforation location and length.

3.3 Effect of natural fracture and hydraulic fracture propagations on oil recovery

Figs. 9(a) and 9(b) illustrate the oil recovery from natural fracture and hydraulic fracture propagations during dynamic spontaneous imbibition. The oil recovery curves of the different models show a similar trend in the initial stage, which can also be observed in the interface evolution with normalized time plots in subsection 3.2. With the progress of spontaneous imbibition, the enhancing effect of hydraulic fracture propagations on hydraulic conductivity and the imbibition duration gradually become apparent. In the models without natural fracture, the eventual oil recoveries of NF0-HF0, NF0-HF200, NF0-HF300, and NF0-HF600 were 23.24%, 35.96%, 46.61%, and 28.05%, respectively. In the models with the natural fracture, the eventual oil recoveries of NF1-HF0, NF1-HF200, NF1-HF300, and NF1-HF600 were 21.67%, 45.53%, 49.72%, and 35.58%, respectively. However, the oil recovery of NF0-HF600 and NF1-HF600 was large compared to the NF0-HF0 and NF1-HF0 models but small compared to the NF0-HF200, NF1-HF200, NF0-HF300, and NF1-HF300 models. Especially compared with the NF1-HF300 model in Fig. 9(b), the eventual oil recovery of the NF1-HF600 model was as much as 14.14% higher and the seepage time was three times longer. Notably, the hydraulic fracture propagation leading to the connection of the primary hydraulic fracture accelerated the drainage rate of oil phase. This phenomenon suggests that such hydraulic fracture propagation could shorten the recovery period but with an accompanying loss of oil recovery. According to the differential pressure curves of the NF1-HF600 model, the oil phase was discharged periodically, which is also seen in the recovery curves. This phenomenon was also

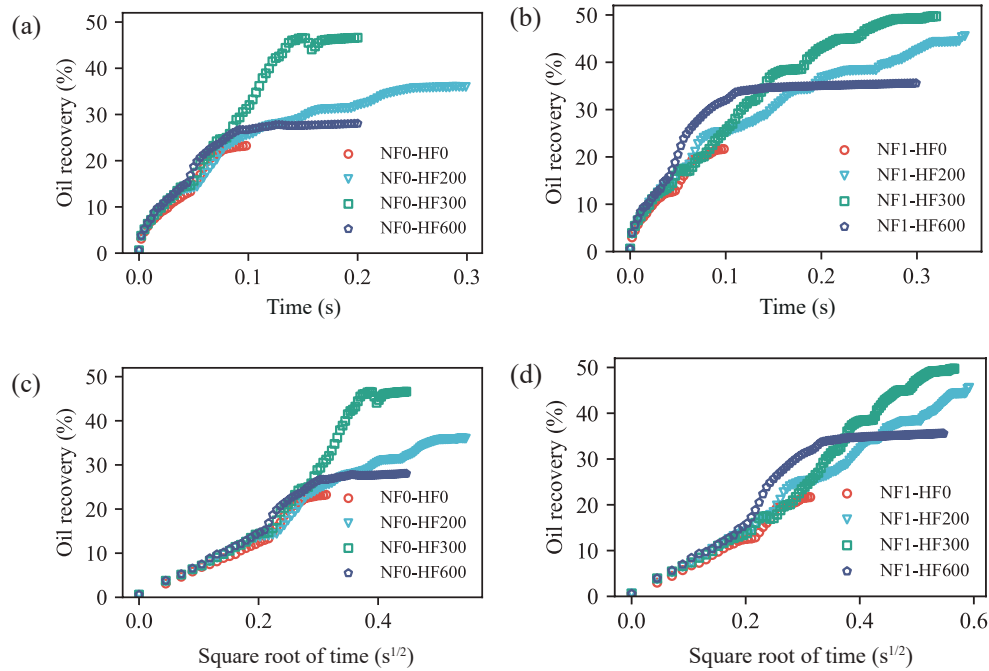


Fig. 9. The imbibition time and the square root of the imbibition time as a function of the oil recovery for all models using the natural fracture as a differentiation criterion: (a) and (c) are the models without the natural fracture; (b) and (d) are the models with the natural fracture.

observed in the interface evolution with normalized time plots in subsection 3.2, indicating that hydraulic fracture propagations increase the oil recovery in the spontaneous imbibition process, albeit this effect is not linear with time. Figs. 9(c) and 9(d) show the oil recovery as a function of the square root of the absorption time. The oil recovery of the NF0-HF0 and NF1-HF0 models was linearly related to the square root of the imbibition time before reaching a steady state, consistent with the experimental results of Rangel-German and Kovscek (2006). However, this linear relationship was periodic in the models, including hydraulic fracture propagations (Figs. 9(c) and 9(d)).

Fig. 10 illustrates the effect of the natural fractures in the matrix on oil recovery. The variability in recovery rates in Fig. 10(a) reflects that the natural fracture impeded imbibition. When the imbibition swept area touches a natural fracture, the oil phase inside the natural fracture cannot be discharged out of the matrix through the narrow pore space by the capillary force alone due to the diameter of the natural fracture being much larger than the pore diameter inside the matrix. Hydraulic fracture propagations can effectively develop the hydraulic conductivity of natural fractures to be used as imbibition channels, expanding the swept area, prolonging the imbibition duration and improving the oil recovery. From Fig. 10(c), the oil recovery shows periodicity with imbibition time, with a decreasing and then increasing trend in each fluctuating stage. This law was also observed in the work by Liu et al. (2020) and He et al. (2022a).

4. Conclusions

This study aimed to compare the effects of natural fracture and hydraulic fracture propagation on spontaneous imbibition in porous media. Porous media models were generated to resemble the spatial structure of real porous media using a threshold Gaussian random field method, referring to the work of Hyman and Winter (2014). The interfacial evolution of spontaneous imbibition between natural fracture and hydraulic fracture propagation in the two-end open mode was discussed in detail based on the propagation law of hydraulic fracture in porous media, including that in the primary hydraulic fracture and the matrix. Variations in the recovery rates resulting from variability in the matrix structure were also analyzed. The main conclusions obtained are as follows:

- 1) The relationship between the pressure difference curve and the morphology of the discharge oil phase in primary hydraulic fractures can determine the state of the discharged oil phase.
- 2) Once a hydraulic fracture propagates in the matrix, natural fractures can be effective at expanding the transverse swept area. The propagating hydraulic fracture can effectively increase the swept depth.
- 3) When the hydraulic fracture propagation links the upper and lower primary hydraulic fractures, oil recovery is increased compared to the case where hydraulic fracture propagation has not occurred but is reduced compared to the case where hydraulic fracture propagation has occurred.

These conclusions can be extended to macroscopic engi-

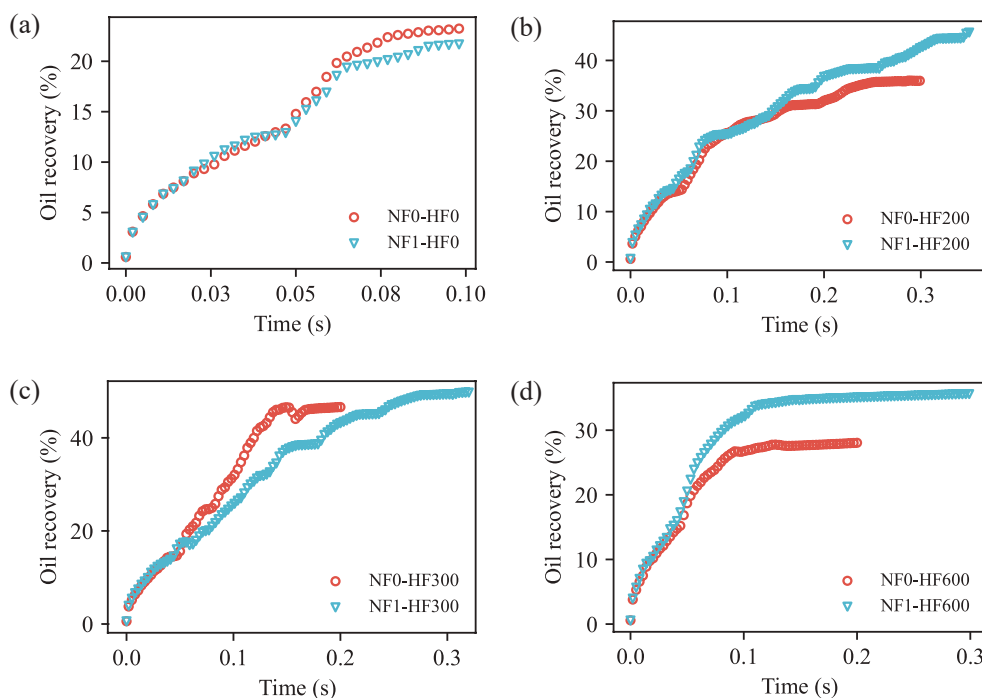


Fig. 10. The imbibition time as a function of the oil recovery for all models using the lengths of the hydraulic fracture propagation as a differentiation criterion. The lengths of the hydraulic fracture propagation are (a) 0 μm , (b) 200 μm , (c) 300 μm , (d) 600 μm , respectively.

neering problems; the trans-layer should be eradicated during hydraulic fracturing, which can lead to a decrease in recovery. Pore filling events such as interfacial coalescence, reverse displacement and Haines jump can be captured by 2D pore-scale simulations; however, corner flows, triggered by the higher pore coordination number of the 3D (three-dimensional) pore structure under strong water-wet conditions, cannot be obtained in 2D pore-scale simulations. With the development of digital core and 3D printing technology, future research should focus on the dynamic spontaneous imbibition processes in 3D pore structures.

Acknowledgements

This work was supported by the National Natural Science Foundations of China (Nos. 41874129, 11972132 and 12272107).

Conflict of interest

The authors declare no competing interest.

Open Access This article is distributed under the terms and conditions of the Creative Commons Attribution (CC BY-NC-ND) license, which permits unrestricted use, distribution, and reproduction in any medium, provided the original work is properly cited.

References

Akhlaghi Amiri, H. A., Hamouda, A. A. Evaluation of level set and phase field methods in modeling two phase flow with viscosity contrast through dual-permeability porous medium. *International Journal of Multiphase Flow*, 2013,

- 52: 22-34.
 Amiri, H. A. A. Pore-scale modeling of non-isothermal two phase flow in 2D porous media: Influences of viscosity, capillarity, wettability and heterogeneity. *International Journal of Multiphase Flow*, 2014, 61: 14-27.
 Berg, S., Ott, H., Klapp, S. A., et al. Real-time 3D imaging of Haines jumps in porous media flow. *Proceedings of the National Academy of Sciences of the United States of America*, 2013, 110(10): 3755-3759.
 Berg, S., van Wunnik, J. Shear rate determination from pore-scale flow fields. *Transport in Porous Media*, 2017, 117: 229-246.
 Blunt, M. J., Bijeljic, B., Dong, H., et al. Pore-scale imaging and modelling. *Advances in Water Resources*, 2013, 51: 197-216.
 Brownscombe, E. R., Dyes, A. B. Water-imbibition displacement-A possibility for the spraberry. *Drilling and Production Practice*, 1952, 7(5): 383-390.
 Cai, J., Hu, X., Standnes, D. C., et al. An analytical model for spontaneous imbibition in fractal porous media including gravity. *Colloids and Surfaces A: Physicochemical and Engineering Aspects*, 2012, 414: 228-233.
 Cai, J., Li, C., Song, K., et al. The influence of salinity and mineral components on spontaneous imbibition in tight sandstone. *Fuel*, 2020, 269: 117087.
 Cai, J., Perfect, E., Cheng, C. L., et al. Generalized modeling of spontaneous imbibition based on Hagen-Poiseuille flow in tortuous capillaries with variably shaped apertures. *Langmuir*, 2014, 30(18): 5142-5151. (in Chinese)
 Cai, J., Yu, B. *Advances in studies of spontaneous imbibition*

- in porous media. *Advances in Mechanics*, 2012, 42(6): 735-754.
- Cai, J., Yu, B., Zou, M., et al. Fractal characterization of spontaneous co-current imbibition in porous media. *Energy & Fuels*, 2010, 24(3): 1860-1867.
- Dahi Taleghani, A., Gonzalez, M., Shojaei, A. Overview of numerical models for interactions between hydraulic fractures and natural fractures: Challenges and limitations. *Computers and Geotechnics*, 2016, 71: 361-368.
- Gao, L., Yang, Z., Shi, Y. Experimental study on spontaneous imbibition characteristics of tight rocks. *Advances in Geo-Energy Research*, 2018, 2(3): 292-304.
- Gruener, S., Sadjadi, Z., Hermes, H. E., et al. Anomalous front broadening during spontaneous imbibition in a matrix with elongated pores. *Proceedings of the National Academy of Sciences of the United States of America*, 2012, 109(26): 10245-10250.
- Guo, J., Li, M., Chen, C., et al. Experimental investigation of spontaneous imbibition in tight sandstone reservoirs. *Journal of Petroleum Science and Engineering*, 2020, 193: 107395.
- Hatiboglu, C. U., Babadagli, T. Oil recovery by counter-current spontaneous imbibition: Effects of matrix shape factor, gravity, IFT, oil viscosity, wettability, and rock type. *Journal of Petroleum Science and Engineering*, 2007, 59(1-2): 106-122.
- He, Z., Liang, F., Meng, J. Pore-scale study of the effect of bifurcated fracture on spontaneous imbibition in heterogeneous porous media. *Physics of Fluids*, 2022a, 34(7): 072003.
- He, Z., Liang, F., Meng, J., et al. Effects of groundwater fluctuation on migration characteristics and representative elementary volume of entrapped LNAPL. *Journal of Hydrology*, 2022b, 610: 127833.
- He, Z., Liang, F., Meng, J. Effects of injection directions and boundary exchange times on adaptive pumping in heterogeneous porous media: Pore-scale simulation. *Science of The Total Environment*, 2023, 867: 161427.
- Hyman, J. D., Winter, C. L. Stochastic generation of explicit pore structures by thresholding Gaussian random fields. *Journal of Computational Physics*, 2014, 277: 16-31.
- Jafari, I., Masihi, M., Nasiri Zarandi, M. Numerical simulation of counter-current spontaneous imbibition in water-wet fractured porous media: Influences of water injection velocity, fracture aperture, and grains geometry. *Physics of Fluids*, 2017, 29(11): 113305.
- Kolawole, O., Ispas, I. Interaction between hydraulic fractures and natural fractures: Current status and prospective directions. *Journal of Petroleum Exploration and Production Technology*, 2020, 10: 1613-1634.
- Lee, J. J., Berthier, J., Theberge, A. B., et al. Capillary flow in open microgrooves: Bifurcations and networks. *Langmuir*, 2019, 35(32): 10667-10675.
- Lei, W., Lu, X., Wu, T., et al. High-performance displacement by microgel-in-oil suspension in heterogeneous porous media: Microscale visualization and quantification. *Journal of Colloid and Interface Science*, 2022, 627: 848-861.
- Li, S., Chen, Z., Li, W., et al. An FE simulation of the fracture characteristics of blunt rock indenter under static and harmonic dynamic loadings using cohesive elements. *Rock Mechanics and Rock Engineering*, 2023, 56(4): 2935-2947.
- Li, C., Singh, H., Cai, J. Spontaneous imbibition in shale: A review of recent advances. *Capillarity*, 2019a, 2(2): 17-32.
- Li, L., Tan, J., Wood, D. A., et al. A review of the current status of induced seismicity monitoring for hydraulic fracturing in unconventional tight oil and gas reservoirs. *Fuel*, 2019b, 242: 195-210.
- Liang, C., Rouzhahong, Y., Ye, C., et al. Material symmetry recognition and property prediction accomplished by crystal capsule representation. *Nature Communications*, 2023, 14(1): 5198.
- Liu, Y., Berg, S., Ju, Y., et al. Systematic investigation of corner flow impact in forced imbibition. *Water Resources Research*, 2022, 58(10): e2022WR032402.
- Liu, Y., Cai, J., Sahimi, M., et al. A study of the role of microfractures in counter-current spontaneous imbibition by lattice Boltzmann simulation. *Transport in Porous Media*, 2020, 133: 313-332.
- Liu, Y., Zou, S., He, Y., et al. Influence of fractal surface roughness on multiphase flow behavior: Lattice Boltzmann simulation. *International Journal of Multiphase Flow*, 2021, 134: 103497.
- Lu, Y., Liu, D., Cai, Y., et al. Spontaneous imbibition in coal with in-situ dynamic micro-CT imaging. *Journal of Petroleum Science and Engineering*, 2022, 208: 109296.
- Lucas, R. Ueber das zeitgesetz des kapillaren aufstiegs von flüssigkeiten. *Kolloid-Zeitschrift*, 1918, 23(1): 15-22.
- Narsilio, G. A., Buzzi, O., Fityus, S., et al. Upscaling of Navier-Stokes equations in porous media: Theoretical, numerical and experimental approach. *Computers and Geotechnics*, 2009, 36(7): 1200-1206.
- Pooladi-Darvish, M., Firoozabadi, A. Cocurrent and counter-current imbibition in a water-wet matrix block. *SPE Journal*, 2000, 5(1): 3-11.
- Prodanović, M., Bryant, S. L. A level set method for determining critical curvatures for drainage and imbibition. *Journal of Colloid and Interface Science*, 2006, 304(2): 442-458.
- Rangel-German, E. R., Kovscek, A. R. A micromodel investigation of two-phase matrix-fracture transfer mechanisms. *Water Resources Research*, 2006, 42(3): W03401.
- Robertson, A. E., Kalidindi, S. R. Efficient generation of anisotropic N-field microstructures from 2-point statistics using multi-output Gaussian random fields. *Acta Materialia*, 2022, 232: 117927.
- Rokhforouz, M. R., Akhlaghi Amiri, H. A. Effects of grain size and shape distribution on pore-scale numerical simulation of two-phase flow in a heterogeneous porous medium. *Advances in Water Resources*, 2019, 124: 84-95.
- Sinton, D. Microscale flow visualization. *Microfluidics and Nanofluidics*, 2004, 1: 2-21.
- Wang, H., Cai, J., Su, Y., et al. Pore-scale study on shale oil-CO₂-water miscibility, competitive adsorption, and mul-

- tipphase flow behaviors. *Langmuir*, 2023, 39(34): 12226-12234.
- Washburn, E. W. The dynamics of capillary flow. *Physical Review*, 1921, 17(3): 273-283.
- Xiong, Q., Baychev, T. G., Jivkov, A. P. Review of pore network modelling of porous media: Experimental characterisations, network constructions and applications to reactive transport. *Journal of Contaminant Hydrology*, 2016, 192: 101-117.
- Yang, C., Liu, J. Petroleum rock mechanics: An area worthy of focus in geo-energy research. *Advances in Geo-Energy Research*, 2021, 5(4): 351-352.
- Yang, Z., Liu, X., Li, H., et al. Analysis on the influencing factors of imbibition and the effect evaluation of imbibition in tight reservoirs. *Petroleum Exploration and Development*, 2019, 46(4): 779-785.
- Zhang, J., Li, Y., Pan, Y., et al. Experiments and analysis on the influence of multiple closed cemented natural fractures on hydraulic fracture propagation in a tight sandstone reservoir. *Engineering Geology*, 2021, 281: 105981.
- Zhou, Y., Guan, W., Cong, P., et al. Effects of heterogeneous pore closure on the permeability of coal involving adsorption-induced swelling: A micro pore-scale simulation. *Energy*, 2022, 258: 124859.
- Zhou, Y., Guan, W., Zhao, C., et al. A computational workflow to study CO₂ transport in porous media with irregular grains: Coupling a Fourier series-based approach and CFD. *Journal of Cleaner Production*, 2023, 418: 138037.
- Zhu, Z., Song, Z., Shao, Z., et al. Simulation of imbibition in porous media with a tree-shaped fracture following the level-set method. *Physics of Fluids*, 2021, 33(8): 082109.